Check for updates

Received: 23 August 2020 | Revised: 6 January 2021 | Accepted: 14 February 2021

DOI: 10.1002/2050-7038.12845

RESEARCH ARTICLE

WILEY

An Experimental Investigation on solar PV fed modular STATCOM in WECS using Intelligent controller

Dishore Shunmugham Vanaja[1] | **Johny Renoald Albert**[2] | **Albert Alexander Stonier**[3]

[1]Electrical and Electronics Engineering, Narayanaguru College of Engineering, Manjalumoodu, Tamil Nadu, India

[2]Electrical and Electronics Engineering, Vivekananda College of Engineering for women, Namakkal, Tamil Nadu, India

[3]Kongu Engineering College, Erode, Tamil Nadu, India

Correspondence
Dishore SV, Electrical and Electronics Engineering, Narayanaguru College of Engineering, Manjalumoodu, Tamil Nadu, India.
Email: dishore312@gmail.com

Summary

This paper describes an optimal way to produce and utilize green power with better energy efficiency. The power quality issues in wind energy conversion systems (WECS) are improved by implementing a photovoltaic (PV) based modular statcom. Modular statcom consist of a modular multilevel inverter (MMI). The peculiar feature of the MMI is that it does not need any auxiliary circuit to provide the negative voltage levels. It is inherent in nature. The DC link of the modular statcom is fed from the PV source, battery, and Flywheel. The excess power obtained from PV and WECS is stored in the battery and Flywheel. Continuous power can be supplied to the load without any interruption is an added advantage of the proposed system. A landsman converter is implemented for the proposed PV system to provide regulated and constant DC supply to the modular statcom. An enhanced second order generalized integrator (ESOGI) with fuzzy logic controller (FLC) is employed to extract the source reference current signal and produce gating pulses for the modular statcom. To verify the performance of the PV-integrated modular statcom, the simulation and experimental studies are performed under specific load conditions. Results show that the proposed system with the ESOGI method reduces the current distortions and satisfies the IEEE-519 standards.

KEYWORDS

solar photovoltaic, wind conversion system, enhanced second order generalized integrator, fuzzy logic controller, total harmonic distortion

List of Symbols And abbreviations: P_m, wind power equation; ρ, intensity of air; N_L, number of levels; V_p, peak voltage; r, radius of turbine; v, velocity of wind; Cp, power coefficient; λ, tip velocity proportion; β, pitch angle; ω, angular velocity; η, diode ideality factor; k, Boltzmann constant; q, electron charge; φ, irradiance; Tc, cell temperature; egap, band gap; Nc, number of cells in series of the PV module; Cpv, overall heat capacity of the PV module; Kin, transmittance absorption factor of PV module; Kloss, overall heat loss coefficient; Ta, ambient temperature; A, is the area of the PV module; V_t, terminal voltage; $Q_{pa}Q_{pb}Q_{pc}$, in-phase voltage template; $Q_{qa}Q_{qb}Q_{qc}$, quadrature voltage template; v_{sab}, $v_{sbc}v_{sca}$, source voltages; I_{loss}, loss component; I_{qq}, current component; R_p, shunt resistance; R_s, series resistance; CCM, continuos conduction mode; DC, direct current; ESOGI, enhanced second order generalized integrator, fuzzy logic controller; FACTS, flexible AC transmission system; FC, fundamental component; MPPT, maximum power point tracking; PCC, point of common coupling; PV, photovoltaic; QSG, quadratic signal generator.; S/H, sample and hold; SEIG, self-excited induction generator; THD, total harmonic distortion; WECS, wind energy conversion systems; ZCD, zero crossing detector.

 © 2021 John Wiley & Sons Ltd.

1 | INTRODUCTION

The demand for utilization of electrical energy for various loads is increasing day by day. Renewable energy sources are combined with the present electrical energy systems to meet the energy demand.[1] Among the renewable energy sources, wind and solar plays a prominent role in generation of electrical power. However, the intermittent nature of solar power affects the grid and reactive load.[2]

PV power does not have a continuous power source because of its intermittent nature. The intermittent problem is avoided by introducing battery storage systems. These energy sources combine to supply flexible energy to satisfy long-term peak demand. Continuous load demand is fulfilled with the establishment of hybrid systems. These hybrid systems play a crucial role in satisfying the demand for the load in the modern distribution system. Among renewable resources, wind power is one of most efficient one.[3] Wind energy plays an important role in reducing power demand. Conventional power plants primarily use synchronous generators to produce electricity. The induction generators are however particularly suitable for the standalone wind energy conversion systems. Induction generators have more advantages than synchronous generators. These benefits include automatically shutting down without causing any damage to the system, good dynamic response, and the ability to produce power at different speeds. The SEIG (self-excited induction generator) works independently without considering the load, making it much more efficient than other generators. The shortcomings of SEIG are that it does not have lower voltage control and does not have enough frequency regulation. To maintain the voltage and frequency in a particular range, FACT (flexible AC transmission systems) devices should be mounted in between the SEIG and load. The term FACT devices imply applying the effectiveness of power electronic converters in the distribution system, especially for handling several power quality issues. The PV system is fed by the power converter to the distribution grid to provide a continuous power supply. Nevertheless, the simultaneous switching of non-linear loads disrupts the connected grid system.[4] This can cause an imbalance of the line voltage, the voltage sag, voltage swell, grid failure, and ultra-low frequency oscillations, harmonics that can damage sensitive loads. The ultra-low frequency oscillations can be reduced by implementing a high-order polynomial structure.[5] Therefore, the FACT devices are to be implemented in the PV system to inject active power to the grid. Selecting the correct mitigation device is relatively easy for basic load applications. Statcom is an important compensatory circuit which is used to compensate voltage-based distortions in the electrical distribution system.[6] Zhang et al.[7] have focused in implementing a damping controller for the statcom in wind farms. Samala and Rosalina[8] investigated the performance monitoring of the controllers for statcom in WECS using the FLC controller which tends to reduce the voltage fluctuation and ensure the stability of the system. An online-based coordinated control of the PV inverter in a grid connected system is implemented in Reference 9. The implemented learning algorithm regulates the output voltage of the inverter effectively. In order to regulate the load side voltage, statcom is installed at the point of common coupling in the power grid between the source and the connected load. This paper explores the concept of integrating a PV-assisted modular statcom with WECS to supply continuous power to the load without any interruption and also to remove the harmonics at the point of common coupling (PCC) using intelligent controller. The paper is organized as follows: Section 2 discusses about the proposed system, Section 3 discusses about the design of the proposed system, Section 4 discusses about the control method implemented for the proposed system, Section 5 discusses about the results and then Section 6 discusses about the conclusions.

2 | PROPOSED SYSTEM

Energy production from wind can help to reduce the power demand. Overall, most traditional power plants use synchronous generators to generate power but the wind energy conversion system uses induction generators. The induction generators have general benefit over regular synchronous generators. The advantages include a brush less durable design, lower costs, less maintenance, simple operation, automatic failure protection, excellent dynamic response, and the ability to generate electricity at different speeds. The preliminary issues of SEIG system include the poor frequency and voltage control. There should be a FACT device unit to track the voltage and frequency in the system in order to keep them stable. The use of FACT device in power system ensures smooth changes in voltage, frequency, and reactive power under the varying loads. The voltage instability found in this system is because of the variations in the load. In this case, statcom and SVC are used to compensate for reactive power in the device. The statcom must have the ability to regulate the voltage obtained from the WECS and effectively match that voltage with the peak power demand. Statcom does not have the tendency to explicitly provide active power supply compensation for a long period of time therefore alternative power supply is made from energy storage devices like battery or ultra-capacitor. Photovoltaic

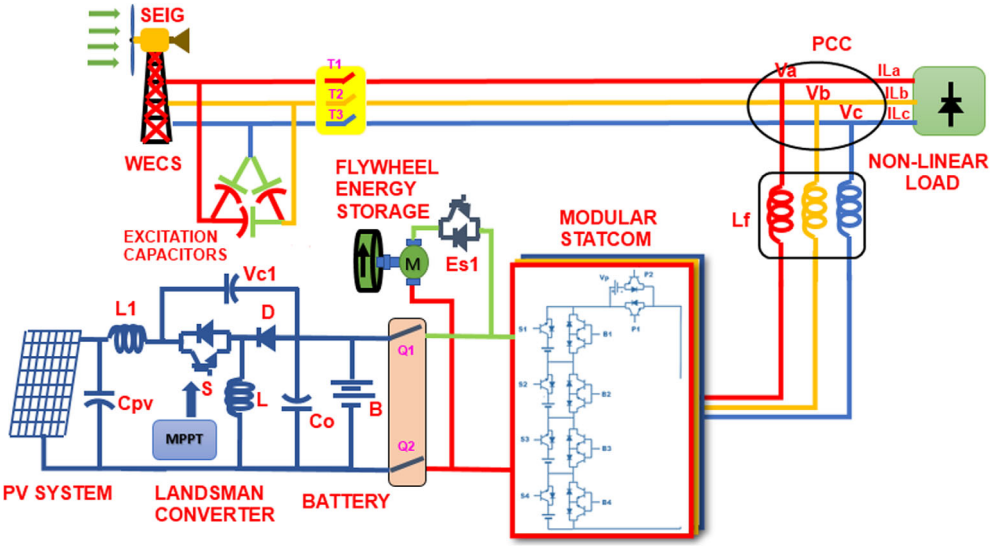


FIGURE 1 Proposed WECS integrated with PV-based modular STATCOM

(PV) power generation would be an additional DC source for statcom, enabling it to improve its voltage management capabilities during power disruptions. The proposed device has a flywheel, which acts like a secondary energy storage unit. The excess power obtained from the WECS is stored in the flywheel in the form of mechanical energy.

The suggested topology uses the renewable energy source with additional energy storage systems to fulfill the DC-link voltage requirements of modular statcom. Figure 1 shows the diagram of the proposed system. The proposed system consists of photovoltaic power generation system, Modular statcom, SEIG, DC machine, and Flywheel. The PV panel, Landsman converter, charge controller, and battery unit are included in the PV power generation system. In the PV power generation system, the landsman converter supplies constant DC power to the DC-link of the modular statcom. During excess generation of power from SEIG the chopper switch ES_1 is activated. On activating the chopper, switch the DC motor begins to transform this excess electric energy into mechanical energy and stores it in the flywheel. This accumulated power in the flywheel is again used to operate the wind turbine when natural wind is not available.

2.1 | Operation of the proposed system

There are five modes of operation of the proposed system. Table 1 shows the modes of operation of the proposed system. They are the wind power mode, PV power mode, battery mode, continuous power supply mode and the flywheel storage mode.

2.1.1 | Wind power mode (Stand-alone operation of WECS)

The first mode is the wind power mode in which the wind energy is being harvested using the wind turbine which is coupled to a SEIG. By triggering the switches T1, T2, T3, the electrical energy produced from the WECS is transferred

TABLE 1 Modes of operation of the proposed system

	Switching States					
Operating Modes	**T1**	**T2**	**T3**	**Q1**	**Q2**	**Es1**
Generation of wind power	✓	✓	✓	×	×	×
Generation of PV power	✓	✓	✓	✓	✓	×
Battery power	✓	✓	✓	✓	✓	×
Continuous supply	✓	✓	✓	✓	✓	×
Flywheel energy storage	✓	✓	✓	×	×	✓

to the load. The load which is non-linear in nature causes harmonics in the system. Among the harmonics, the lower order harmonics are very dangerous and cause failure in the components of WECS resulting in a total damage of the system. For mitigating the harmonics and maintain a good power quality at the point of common coupling, a PV-based modular statcom is implemented in the WECS.

2.1.2 | PV power mode

In the PV power mode, the solar energy is being trapped by the PV panels and is given to the landsman converter.[10] From the landsman converter, the regulated DC voltage is stored in the battery. The landsman converter is operated with P&O (perturb and observe) MPPT (maximum power point tracking) controller[11] to extract maximum power from the PV panels. Since solar energy is not available during the night and for continuous operation of the system, a battery energy storage system is very much essential for the proposed system. The PV power generation system is used as a harmonic compensator and reactive power compensator by incorporating the modular statcom.

2.1.3 | Battery mode

When there is absence of sunlight, the proposed system works in the battery mode. Since the PV system depends upon the weather conditions and due to uneven radiations, the power from the PV panel fluctuates. This fluctuated power is dangerous if it is fed to the inverter or used for the DC loads. Therefore, a battery must be incorporated in the PV system to provide continuous and constant DC power to the load.

2.1.4 | Continuous power supply mode

In this mode, the continuous power supply is given to the load when there is any fault or maintenance in the wind energy conversion system. The switches T1, T2, T3 are turned off and the load gets power from the PV system. In this mode of operation based on the weather conditions both the PV system as well as the battery can feed the supply to the load.

2.1.5 | Flywheel storage mode

This mode is operated when the WECS produces excess amount of energy. During this mode, the switches Q1 and Q2 are opened so that the PV system is isolated from the entire system. By turning on the switch E_S1, the DC motor rotates and stores the excess energy produced by the WECS in the flywheel. If wind is not available to produce power, then the energy stored in the flywheel can be used for operating the load as well as can be used to run the turbine.

3 | DESIGNING OF PROPOSED SYSTEM

3.1 | Wind generator

Wind turbine produces power by driving the generator using the wind energy. The wind flows over the blade to generate a lifting and turning force. The blade rotates a shaft placed in the nacelle, which in turn is connected with a gearbox. Further, the gearbox boosts the rotating speed of the generator, from which it utilizes the magnetic field to change the mechanical power into electric power.

The generated wind power equation is shown below

$$P_m = 0.5C_p(\lambda,\beta)\rho\pi r^2 v^3 \tag{1}$$

Here intensity of air is denoted as ρ, radius of turbine blade is denoted as r, wind velocity is denoted as v, and power coefficient is denoted as C_p, which depends on tip velocity proportion is denoted as λ and pitch angle is denoted as β.

The tip velocity proportion is expressed as

$$\lambda = \frac{\omega r}{v} \tag{2}$$

where angular velocity of generator is denoted as ω.

Tip velocity proportion λ is noticed from Equation (2) and varied by adjusting the velocity ω, resulting in the controlling of the power coefficient C_p, and generated power output from the wind turbines.

3.2 | PV system

A photovoltaic cell is the key component of the photovoltaic network,[12] consisting of multiple series/parallel attached photovoltaic cells for each module. Since the PV module contains non-linear features, it is necessary to develop a PV module to make the exact design, function, and identification of causes of PV output degradation. Any minor variation of Rs has a significant effect on the output of PV cell. A single PV panel is made up of 24 solar cells. Each solar cell has an open-circuit voltage of 0.5 V. There are 24 solar cells in a single panel. These solar PV cells are combined in series to the produce 12 V, 7 A at standard test conditions (1000 W/mm^2 and 25°C). To achieve a voltage of 24 V and a current of 7 A at the output from the solar PV system, two 12 V, 7 A modules are fixed in series.

From Figure 2,

$$I = I_L - I_D \tag{3}$$

where I presents the output current, I_L presents the light current, and I_D presents the diode current.

From Schottky equation, the current passing through the diode is given as

$$I_D = I_o\left[\exp\left(\frac{U + IR_s}{nkT/q}\right) - 1\right] \tag{4}$$

where I_o is the reverse saturation current, η is the diode ideality factor, k is the Boltzmann constant ($k = 1.38 \times$ e-23 J/K), q is the electron charge (1.6×10^{-19} C), T is the solar PV array operating temperature (1000 W/m^2, 25°C. For Si solar cell of 25°CnkT/q = 0.0259 volts = α

$$I_D = I_o\left[\exp\left(\frac{U + IR_s}{\alpha}\right) - 1\right] \tag{5}$$

Substituting Equation (5) in Equation (3)

$$I = I_L - I_o\left[\exp\left(\frac{U + IR_s}{\alpha}\right) - 1\right] \tag{6}$$

In Equation (6), the light current is presented as

$$I_L = \frac{\phi}{\phi_{\text{ref}}}[I_{\text{L,ref}} + \mu_{I.SC}(T_c - T_{\text{c,ref}})] \tag{7}$$

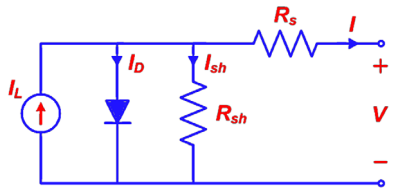


FIGURE 2 Equivalent circuit of PV panel

where φ represents the irradiance, φ_{ref} represents the reference irradiance, $I_{L\text{ref}}$ presents the reference light current, T_c gives the cell temperature, and T_{cref} gives the reference cell temperature.

The saturation current I_o is determined by Equation (8)

$$I_o = I_{o,ref}\left(\frac{T_{c,ref}+273}{T_c+273}\right)^3 \exp\left[\frac{e_{\text{gap}}N_s}{q\alpha_{\text{ref}}}\left(1-\frac{T_{\text{c,ref}}+273}{T_c+273}\right)\right] \tag{8}$$

where I_{oref} is the reference saturation current, e_{gap} is the band gap of the silicon material (1.17 ev), N_{c} is the number of cells in series of the PV module, q is the electron charge

$$I_{o,ref} = I_{L,\text{ref}}\exp\left(-\frac{U_{\text{0c,ref}}}{\alpha_{\text{ref}}}\right) \tag{9}$$

$U_{\text{oc,ref}}$ is the open circuit voltage of the PV module, α_{ref} can be calculated using Equation (10).

$$\alpha_{ref} = \frac{2U_{mp,ref}-U_{oc,ref}}{\frac{I_{sc,ref}}{I_{sc,ref}-I_{mp,ref}}+\ln\left(1-\frac{I_{mp,ref}}{I_{sc,ref}}\right)} \tag{10}$$

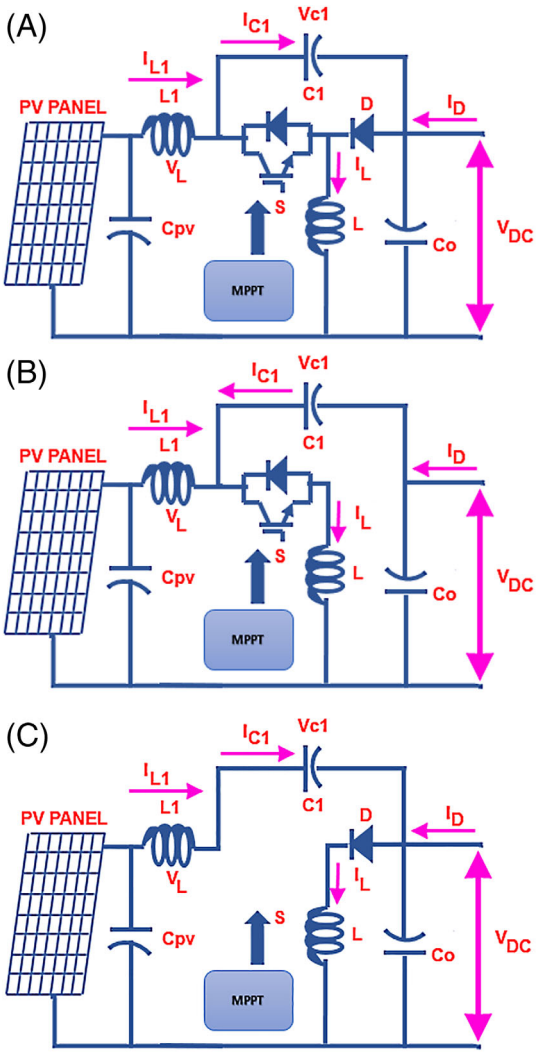


FIGURE 3 Landsman Converter (A) circuit (B) Mode I (C) Mode II

where α is a function of temperature and is presented as

$$\alpha = \frac{\mathrm{T_c} + 273}{T_{c,\mathrm{ref}} + 273}\alpha_{\mathrm{ref}}$$

The series resistance can be calculated using Equation (11)

$$R_s = \frac{\alpha_{\mathrm{ref}} \ln\left(1 - \frac{I_{mp,\mathrm{ref}}}{I_{\mathrm{sc,ref}}}\right) + U_{\mathrm{oc,ref}} - U_{\mathrm{mp,ref}}}{I_{\mathrm{mp,ref}}} \tag{11}$$

The thermal model of PV module is presented in Equation (12)

$$C_{pv}\frac{dT_c}{dt} = k_{in,pv}\phi - \frac{U \times \mathrm{I}}{A} - K_{\mathrm{loss}}(T_c - T_a) \tag{12}$$

where C_{pv} is the overall heat capacity of the PV module, K_{in} is the transmittance absorption factor of PV module, K_{loss} is the overall heat loss coefficient, T_{a} is the ambient temperature, and A is the area of the PV module.

3.3 | Landsman converter

Landsman converter is a DC-DC converter which operates in continuous conduction mode (CCM). As the solar radiation varies, the outputs of the PV array are not accurate. To feed constant DC power without any interruption or oscillation a Landsman converter is implemented in the proposed PV generation system. Figure 3A presents the Landsman converter. It has two modes of operation.

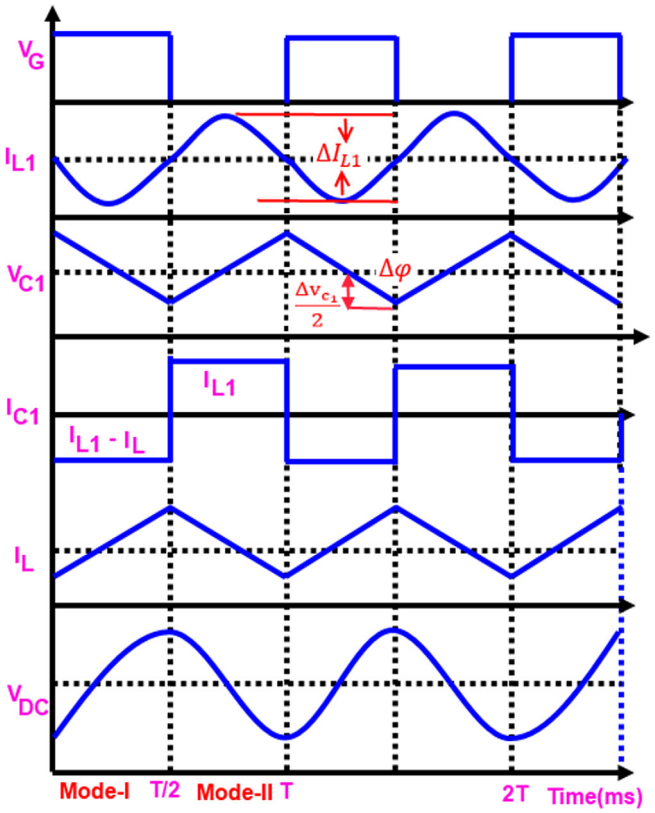


FIGURE 4 Waveform of the landsman converter

3.3.1 | Mode I

When switch **S** is triggered, the diode **D** in the circuit is reverse biased. The current in inductor flows through switch **S** and it is denoted as $\mathbf{I_L}$. The potential across the intermediate capacitor $\mathbf{C_1}$ is denoted as $\mathbf{VC_1}$. If $\mathbf{VC_1}$ is greater than the output voltage $\mathbf{V_{DC}}$, then the intermediate capacitor $\mathbf{C_1}$ discharges through the switch **S** to **L**, and then inductor **L** transfers the energy finally to the output. So, voltage across intermediate capacitor $\mathbf{VC_1}$ reduces and inductor current $\mathbf{I_L}$increases. Therefore, the input supplies the energy to input inductor $\mathbf{L_1}$. Figure 3B presents the mode I operation.

3.3.2 | Mode II

When switch is opened, the diode D is forward biased. The current from the inductor I_L flows through the diode. From the diode, the energy stored in inductor L transfers its energy to the output side. During this mode, the capacitor $C_1$is charged by means of stored energy from both input and inductor L_1. So, voltage VC_1 in the intermediate capacitor increases and the inductor current I_L decreases. Figure 3C presents the mode II operation.

3.3.3 | Design of Landsman converter

Figure 4 presents the waveform of the Landsman converter. By considering the continuous conduction mode of operation, the ripples present in inductor current I_{L_1} flows through capacitor C_1. The shaded part in waveform v_{c_1} shows an extra flux $\Delta\Phi$. Thus, peak-to-peak ripple current ΔI_{L_1} is expressed as

$$\Delta I_{L_1} = \frac{\Delta\Phi}{L_1} = \frac{\Delta v_{c_1} T}{L_1 2 \times 2 \times 2} \tag{13}$$

When switch is turned off, the current via C_1 is

$$i_{C_1} = I_{L_1} = C_1 \frac{\Delta v_{c_1}}{(1-D)^T} \tag{14}$$

where *D* is the duty ratio and *T* is the switching period.
The ripple in voltage $v_{c_1}$is calculated from above expression

$$\Delta v_{c_1} = \frac{I_{L_1}}{C_1}(1-D)^T \tag{15}$$

By substituting $\Delta v_{c_1}$from (13) in (15),

$$\Delta I_{L_1} = \frac{I_{L_1}}{L_1 2 \times 2 \times C_1}(1-D)^T \frac{T}{2} \tag{16}$$

$$\Delta I_{L_1} = \frac{1}{8 L_1 C_1} \frac{I_{L_1}(1-D)}{f_{SW}^2} \tag{17}$$

It is normalized as

$$\frac{\Delta I_{L_1}}{I_{L_1}} = \frac{1}{8 L_1 C_1} \frac{(1-D)}{f_{SW}^2} \tag{18}$$

From the input-output relation,

$$I_{L_1} = \frac{D}{1-D} I_{dc} \tag{19}$$

FIGURE 5 (A) Basic structure of the MMI. (B) Basic unit of MMI

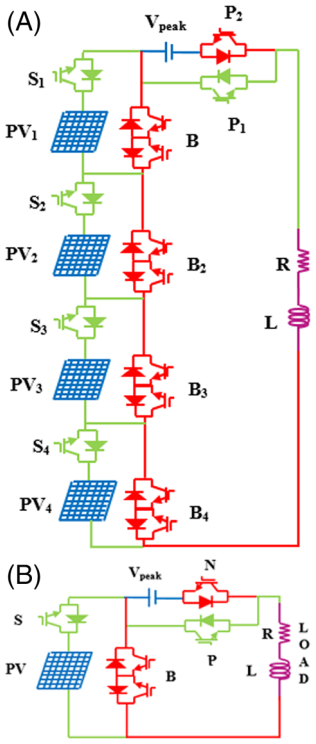


TABLE 2 Equations of the proposed symmetric and asymmetric modular multilevel inverter

Parameters	Symmetric	Asymmetric	Asymmetric
Number of levels	N_L(9-level)	N_L(27 -level)	N_L(31 -level)
Number of unidirectional switches	$(N_L - 3)$	$\frac{N_L+3}{5}$	$\frac{N_L-1}{5}$
Number of bidirectional switches	$(N_L - 4)$	$\frac{N_L+3}{6}$	$\frac{N_L-1}{6}$
Number of diodes	$(N_L + 5)$	$\frac{N_L+1}{2}$	$\frac{N_L-3}{2}$
Number of driver circuit	$(N_L + 5)$	$\frac{N_L-7}{2}$	$\frac{N_L-1}{3}$
Number of DC sources	$(N_L - 4)$	$\frac{N_L-7}{4}$	$\frac{N_L+1}{8}$

where I_{dc} is the output current of Landsman Converter
Substitute Equation (19) in (17),

$$L_1 = \frac{DI_{dc}}{8C_1\Delta I_{L_1}} \tag{20}$$

3.4 | Design of proposed modular statcom

Modular multilevel inverters were designed since it has advantages like reduction in the device count, reduced blocking voltage across the switches, capable of producing symmetric and asymmetric configurations, even power distribution, and modularity. The basic structure and the basic unit of MMI are presented in Figure 5. It consists of four PV sources and the fifth source (Vpeak) is obtained by connecting the four PV sources in series. The PV panels are fed with DC-DC converters to obtain constant voltage at the output. Figure 5B presents the basic unit of the proposed MMI. The basic unit consist of a PV source, three unidirectional switches (S, P, N), a bidirectional switch (B), a peak voltage source (Vpeak), and the RL load. In the basic circuit when switch S is triggered along with switch P the positive voltage level (+PV) is generated. For obtaining the negative voltage level the switches N and B must be

TABLE 3 Switching sequence of the symmetric MMI

S1	S2	S3	S4	B1	B2	B3	B4	P1	P2	Stages of operation	Output Voltage (V_o)
✓	X	X	X	X	✓	✓	✓	✓	X	I	1 V_{DC}
✓	✓	X	X	X	X	✓	✓	✓	X	II	2 V_{DC}
✓	✓	✓	X	X	X	X	✓	✓	X	III	3 V_{DC}
✓	✓	✓	✓	X	X	X	X	✓	X	IV	4 V_{DC}
X	X	X	X	✓	✓	✓	✓	✓	X	XIV	0 V_{DC}
X	✓	✓	✓	✓	X	X	X	X	✓	XV	$-1V_{DC}$
✓	✓	X	X	X	X	✓	✓	X	✓	XVI	$-2V_{DC}$
✓	X	X	X	X	✓	✓	✓	X	✓	XVII	$-3V_{DC}$
X	X	X	X	✓	✓	✓	✓	X	✓	XVIII	$-4V_{DC}$

Note: ✓, ON; **X**, OFF.

TABLE 4 conventional 9-level symmetrical topologies

Topology	N_L	N_{DC}	N_{sw}	N_C	N_D	Negative levels
Babaei[13]	9	4	20	0	20	H-bridge
Chaudhuri & Rufer[14]	9	1	14	4	14	Inherent
Chaudhuri et al.[15]	9	1	14	4	14	Inherent
Jahan et al.[16]	9	1	17	4	21	H-bridge
Proposed	9	5	14	0	0	Inherent

Abbreviations: N_L, number of levels; N_{DC}, number of DC sources; N_{sw}, number of switches; N_C, number of capacitors; N_D, number of diodes.

triggered. When switch N is triggered the peak voltage is activated and is passed through the bidirectional switch (B) with a negative polarity thus the negative voltage level (−PV) is generated. The peak voltage of the basic unit is same as the PV voltage and this condition is only suitable for Figure 5B. This peak voltage value changes when additional units are added . The zeroth level is generated by switching the unidirectional switch P and the bidirectional switch B. Therefore, the basic unit generates a three level of output voltage (+PV, 0 V, −PV). The proposed structure can be operated in both symmetric and asymmetric modes. Table 2 shows the parameters of the proposed MMI. Adding an additional unit to the basic unit can generate a five level of output voltage. If we consider two units where there are two PV sources (PV1, PV2), then the peak voltage or the fifth DC voltage value will be the sum of the PV sources (PV1 + PV2). Likewise, if we take the Figure 5A, the peak voltage of the basic structure is PV1 + PV2 + PV3 + PV4. Therefore by triggering the unidirectional switches (S1, S2, S3, S4) along with the switch P1, the positive voltage levels are obtained and by triggering the unidirectional switches (S1, S2, S3, S4) along with the switch P2, the peak voltage (Vpeak) gets activated and the negative voltage levels are obtained. The proposed structure can be extended to several levels. In the basic structure, if symmetric voltages are implemented, then a 9-level output voltage is generated. If two such modules are connected in a cascaded form, then a 17-level output is generated. Table 3 indicates the strategy of switching for the suggested symmetric MMI. Figure 6 presents the modes of operation of the symmetric MMI.

In the proposed structure, the common emitter configuration of bidirectional switch is used, since it has fewer conduction losses and needs a single gate driver circuit. The suggested configuration is suitable for solar PV applications, since 5 isolated DC sources can be used. Table 4 shows the comparison of the proposed MMI with other reduced switch MLIs .

4 | CONTROL SCHEME OF SOLAR PV-INTEGRATED MODULAR STATCOM

An enhanced second order generalized integrator (ESOGI) based control method is implemented for the proposed system. The role of this algorithm is to retrieve the fundamental component (FC) from the load current and using the FC,

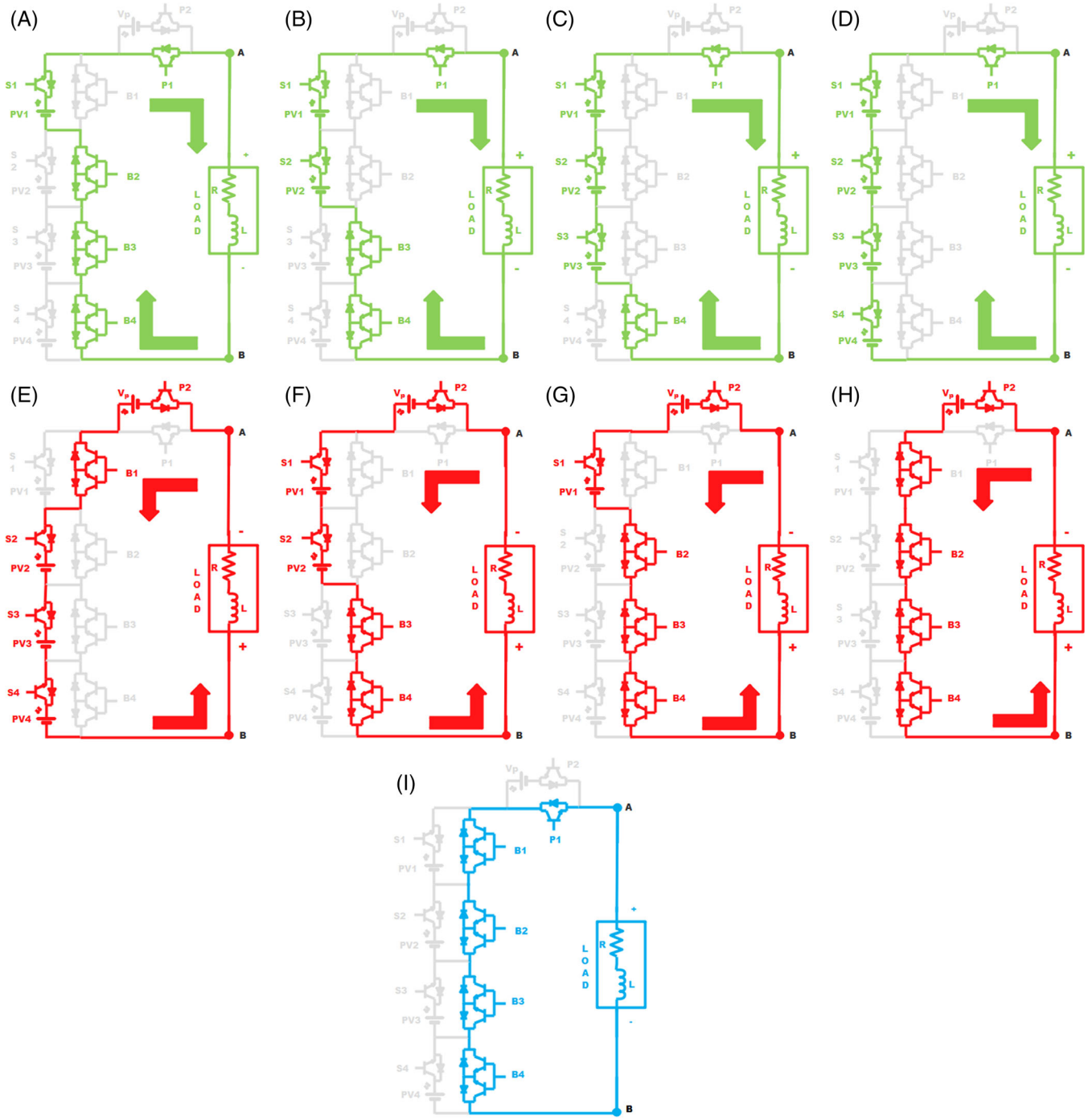


FIGURE 6 (A–I) Modes of operation of the symmetric MMI

the respective reference source currents are produced. These reference source currents are compared with the actual source currents and the error generated is transferred to the hysteresis controller. From the controller, the triggering pulses are obtained for the switches of the modular statcom. Therefore, the harmonic content at the PCC is removed by injecting the same magnitude of harmonic content in the opposite direction from the modular statcom. Figure 7 shows the overall control system of the proposed system. The harmonic content is measured by extracting the in phase and quadrature components of the load currents ($\mathbf{I_{La}}$,$\mathbf{I_{Lb}}$,$\mathbf{I_{Lc}}$). This algorithm uses a quadratic signal generator (QSG) unit, which senses and transfers the errorless phase and frequency signal from the load current to the controller. The ESOGI method is obtained by adding an auxiliary integrator unit to the QSG block. This integrator unit helps to cancel the DC offset current component from the load current. To this auxiliary integrator unit in the QSG, a damping error

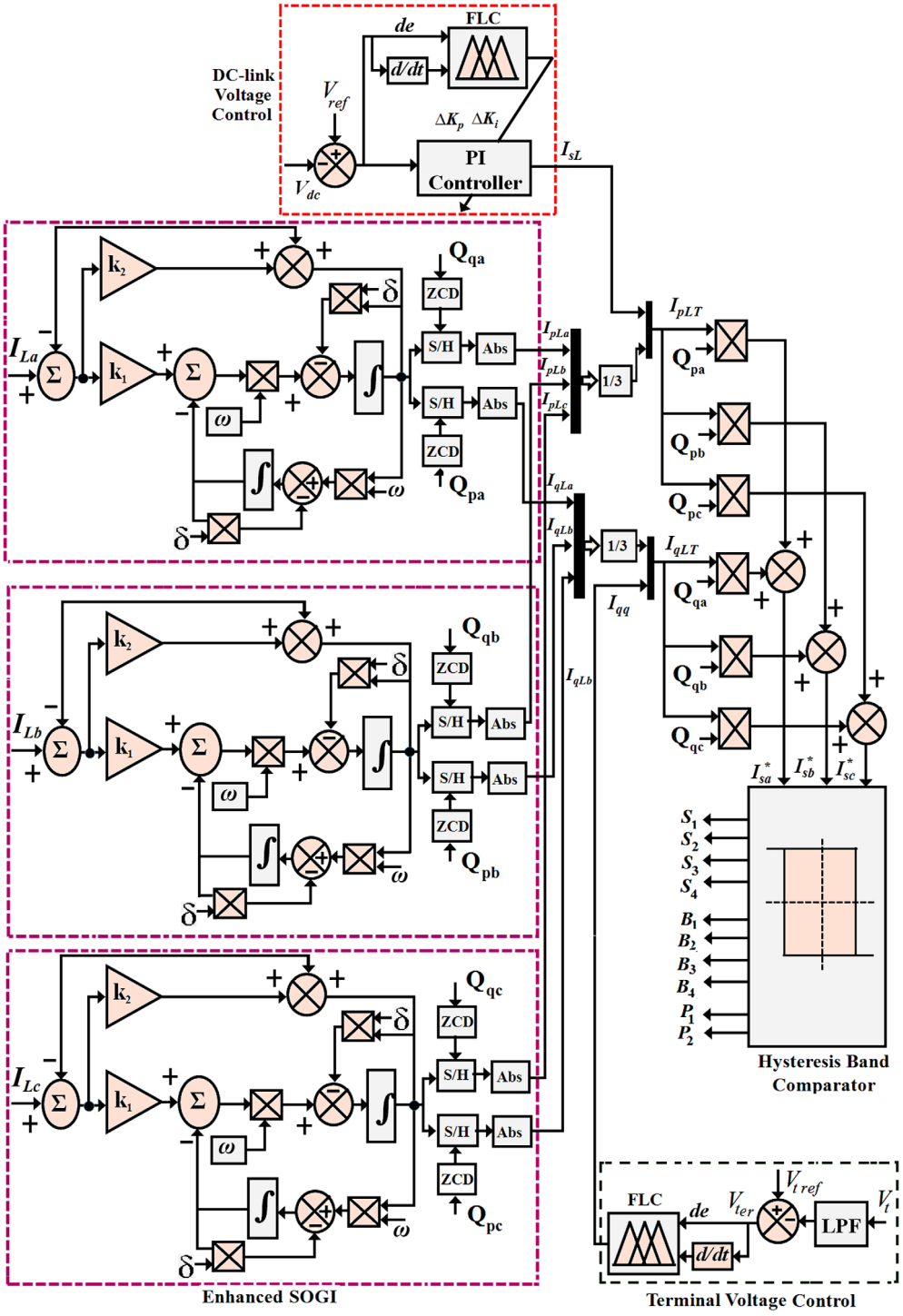


FIGURE 7 Control scheme of modular statcom based on ESOGI with FLC

compensator (δ) is included for error compensation during changes in load. Equation (21) shows the transfer function of the ESOGI method.

$$\mathbf{f_{ESOGI}(s)} = \frac{\omega(s+\delta)}{(s+\delta)^2+\omega^2} \tag{21}$$

where δ is the damping compensator, ω is the angular frequency in rad/s. Larger value of the damping compensator introduces oscillations in the system. Therefore, the damping compensator δ is calibrated to 0.9. This value can be used for any value of the load current.

4.1 | Generation of the reference source currents

The in phase and quadrature components is obtained from Equations (22) and (23)

$$\begin{bmatrix} Q_{pa} \\ Q_{pb} \\ Q_{pc} \end{bmatrix} = \frac{1}{3V_t} \begin{bmatrix} 1 & 0 & -1 \\ -1 & 1 & 0 \\ 1 & -1 & 0 \end{bmatrix} \begin{bmatrix} v_{sab} \\ v_{sbc} \\ v_{sca} \end{bmatrix} \tag{22}$$

$$\begin{bmatrix} Q_{qa} \\ Q_{qb} \\ Q_{qc} \end{bmatrix} = \frac{1}{2\sqrt{3}} \begin{bmatrix} 0 & -2 & 2 \\ -3 & 1 & -1 \\ 3 & 1 & -1 \end{bmatrix} \begin{bmatrix} Q_{pa} \\ Q_{pb} \\ Q_{pc} \end{bmatrix} \tag{23}$$

where, V_t is the terminal voltage, Q_{pa},Q_{pb},Q_{pc} represents the in-phase voltage template, Q_{qa},Q_{qb},Q_{qc} represents the quadrature voltage template and v_{sab}, v_{sbc}, and v_{sca} represents the source voltages (V).

Terminal voltage V_t is calculated using Equation (24).

$$V_t = \sqrt{\frac{2}{3}\left(v_{sa}^2 + v_{sb}^2 + v_{sc}^2\right)} \tag{24}$$

The voltage template of the in phase and quadrature components are compounded with the respective active power component and reactive power component to generate the reference currents.

4.1.1 | DC-link voltage control

For controlling the DC link voltage of the modular statcom, a PI controller is used. A PI controller is a closed-loop or feedback system in which the calculated value of the controlled parameter is fed back to the comparator. The controlled parameter is equivalent to the target value or set-point in the comparator. If there is a variation between the calculated parameter and the set-point, an error is produced. This error approaches the controller, which in return changes the final control element to return the controlled parameter to the set-point. For the control of the DC link voltage, a PI voltage type controller is used. The reference value of the DC link voltage ($V_{DC\ ref}$) is compared with the measured value of the DC link voltage ($V_{DC\ meas}$) and a error is generated. The weighted sum of the error (the difference between

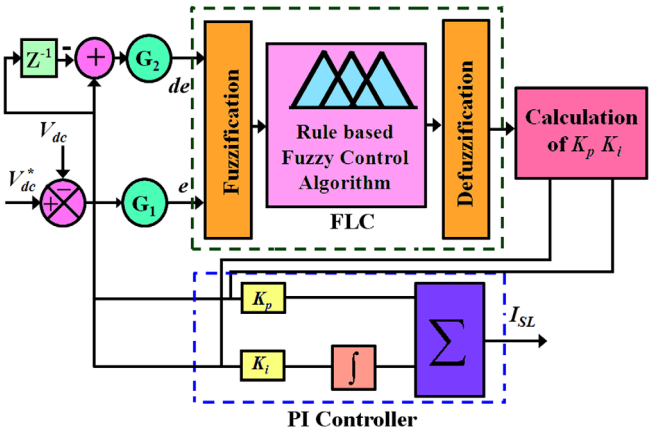


FIGURE 8 Fuzzy tuned PI voltage type of controller

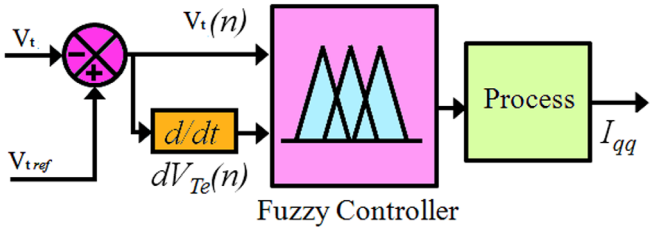


FIGURE 9 FLC based terminal voltage controller

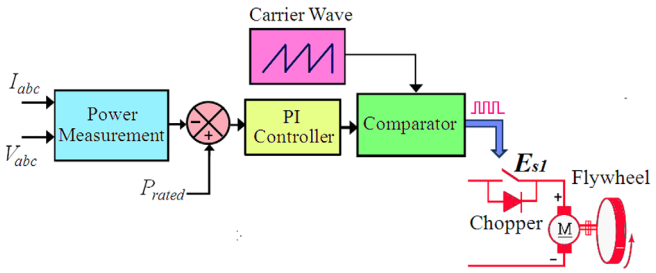


FIGURE 10 flow chart of Pulse generation using ESOGI

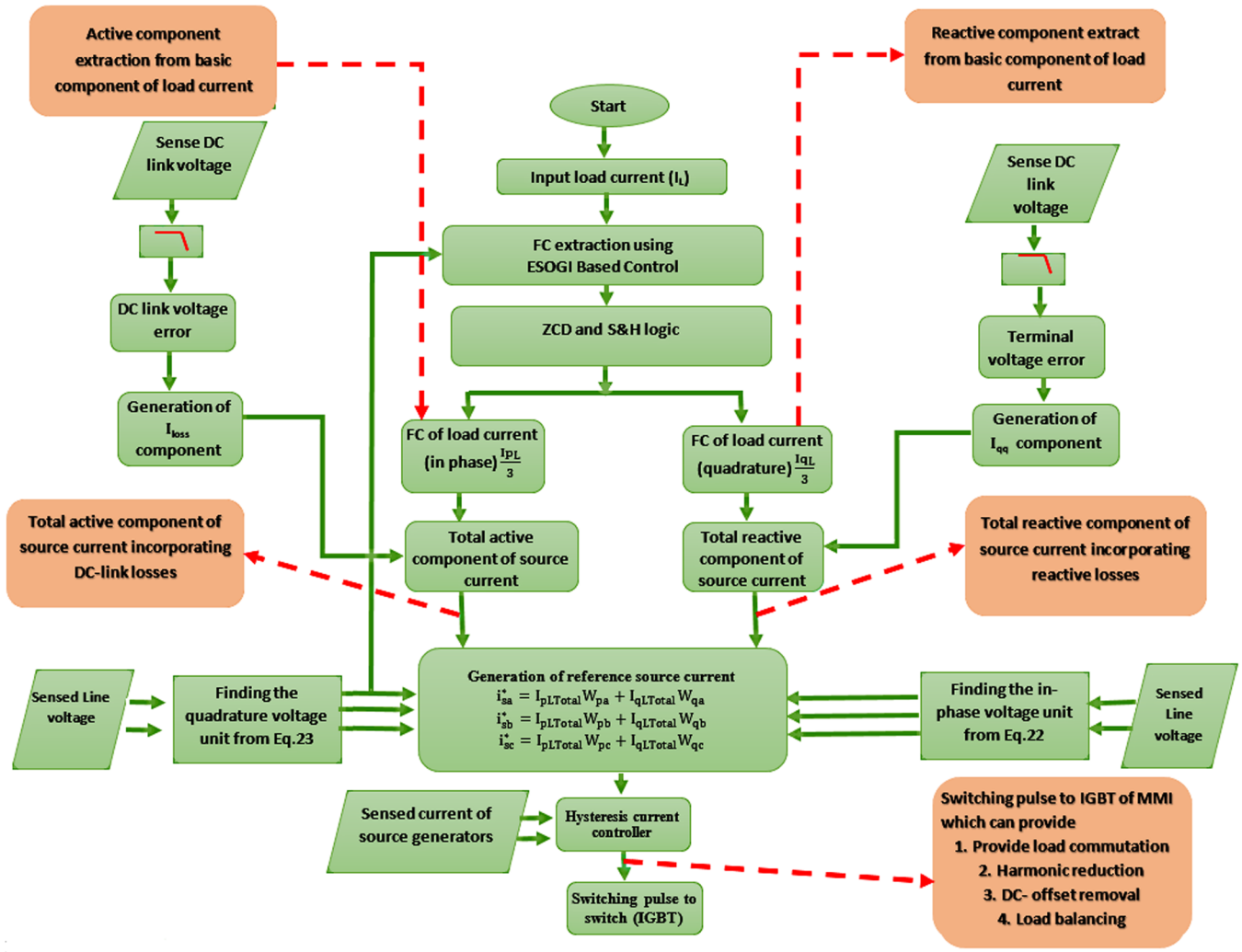


FIGURE 11 Control system for Flywheel energy storage system

TABLE 5 Comparison of various control methods

Parameters	ESOGI	DSOGI	MSOGI	SOGI
Accuracy	High	Medium	Medium	Less
Complexity	Low	Medium	Medium	Low
DC offset rejection	Yes	Yes	Yes	No
Filter type	Band pass	Band pass	Band pass	Low pass filter
Extraction of FC	Low	Medium	Medium	High
Memory requirement	Low	High	High	Low
No. of integrators used	3	4	6	2

TABLE 6 Simulation parameters

Parameters		Value
Three-phase (Phase voltage)		230 V
Frequency		50 Hz
DC-link Voltage	^{V}dc	600 VV
DC-link capacitors	^{C}dc	2200 μF
Filter	*Lf*, Cf, *Rf*	5 mH, 80 μF, 1.5 Ω
Switching frequency	*fs*	10 Hz
Injection transformer		400 V/400 V, 3 kVA
Self-excited induction generators		
Voltage	VL/Vph	400 V/230 V
No. poles	P	4
Rated rotor speed	N	1410 rpm
Flywheel		
Rated energy	R	10 Kw
Rated speed	N_f	1500 rpm
Diameter	D	500 mm
Modular Statcom		
IGBT	Switches	14
PV Sources	4	150 V_{DC}
Switching frequency	^{f}sf	20 kHz
PV system		
No. of SPV cells		6 × 10
Nominal SPV voltage		12 V
Maximum power	^{P}mp	230 W
Voltage at Pmp	^{V}mp	35.5 V
Current at Pmp	^{I}mp	6.77 A
Open circuit voltage	^{V}oc	43.6 V
Short circuit current	^{I}sc	7.37 A
Battery capacity	B	500 Ah
Non-linear load		
Three-phase converter	*LL*	3 mH
	^{L}DC	5.7 mH
	^{R}DC	12 Ω

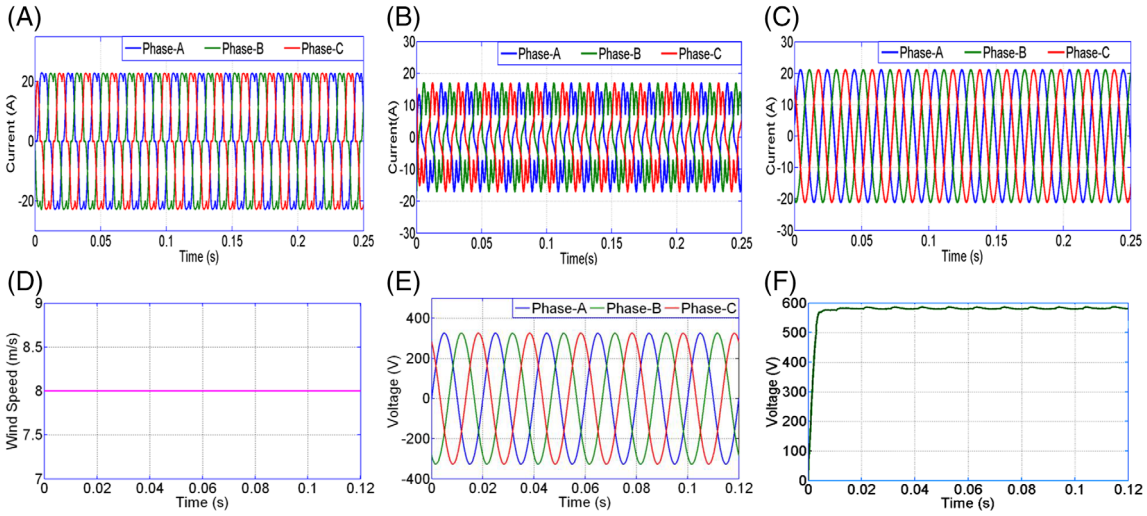


FIGURE 12 (A) Load current; (B) injected compensation current from modular statcom; (C) source current; (D) wind speed; (E) source voltage; and (F) DC-link voltage of the modular statcom

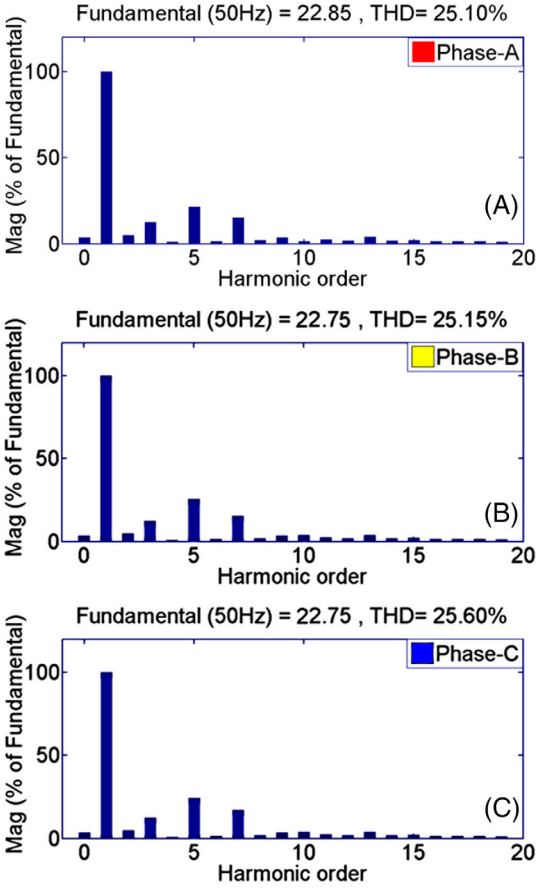


FIGURE 13 (A–C) Harmonic distortion of load current before connecting the modular statcom

output and target setpoint) and the integral value can be controlled by this PI Voltage controller. The gains of the PI controller are tuned using fuzzy system.[17] But if the gains of the PI controller are determined by trial and error, the steady-state error problems occur. Figure 8 shows the diagram of the Fuzzy tuned PI voltage type of controller for the control of DC link voltage.

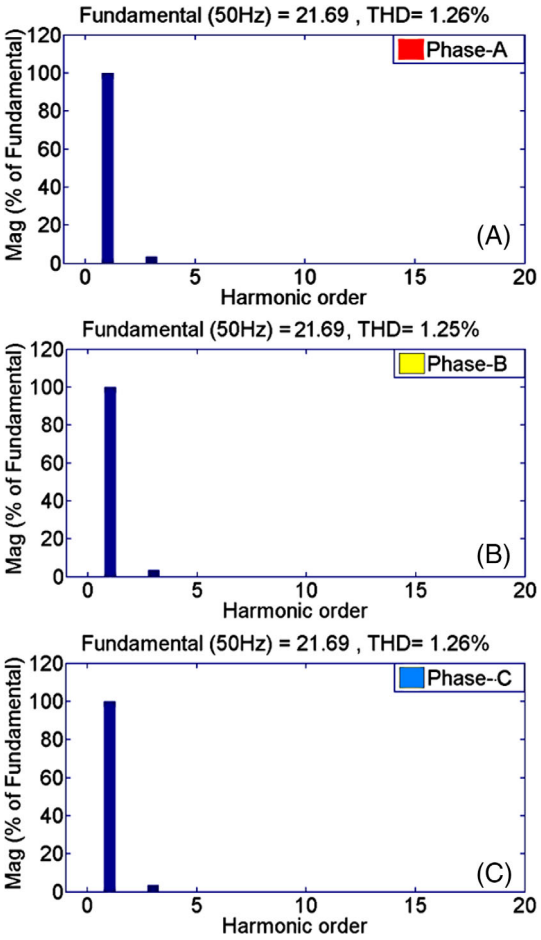


FIGURE 14 (A,B) Harmonic distortion of load current after connecting the modular statcom

$$V_{DC\ link\ error}(p) = V_{DC\ ref}(p) - V_{DC\ meas}(p) \tag{25}$$

The error signal is processed and the loss component I_{loss} is obtained. I_{loss} can be calculated using Equation (26).

$$I_{loss}(p) = I_{loss}(p-1) + k_{pDC}\{V_{DC\ link\ error}(p) - V_{DC\ link\ error}(p-1)\} + k_{iDC}(p)V_{DC\ link\ error}(p) \tag{26}$$

4.1.2 | Terminal voltage control

The terminal voltage reference value ($V_{t\ ref}$) is compared with the measured terminal voltage value ($V_{t\ meas}$) to estimate the error voltage ($V_{t\ error}$).

$$V_{t\ error}(p) = V_{t\ ref}(p) - V_{t\ meas}(p) \tag{27}$$

This error voltage ($V_{t\ error}$) is sent to a Fuzzy type PI controller, which decides the current component I_{qq} for PCC terminal voltage control. I_{qq} can be calculated using Equation (28).

$$I_{qq}(p) = I_{qq}(p-1) + k_{ptDC}\{V_{DC\ link\ error}(p) - V_{DC\ link\ error}(p-1)\} + k_{itDC}(p)V_{DC\ link\ error}(p) \tag{28}$$

Figure 9 shows the FLC based terminal voltage controller. The $I_{loss}$and I_{qq}components are the important parameters used to calculate the total active and reactive current components of the source. By adding the I_{loss}component with the active component of the load current, the net active current component ($I_{p\ total}$) is obtained. By adding the I_{qq}component with the active component of the load current, the net reactive current component($I_{q\ total}$) is obtained.

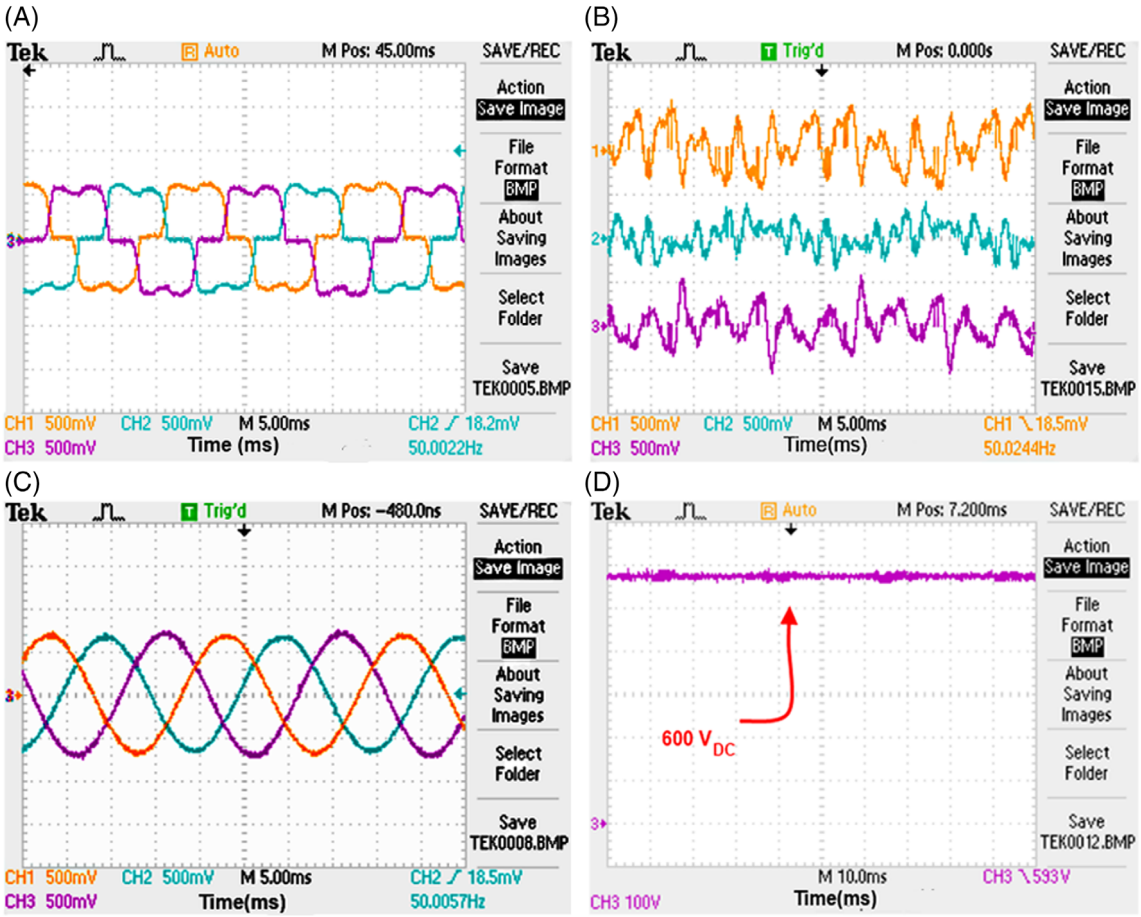


FIGURE 15 Experimental output of (A) load current; (B) injected compensation current from modular statcom; (C) source current; and (D) DC-link voltage of the modular statcom

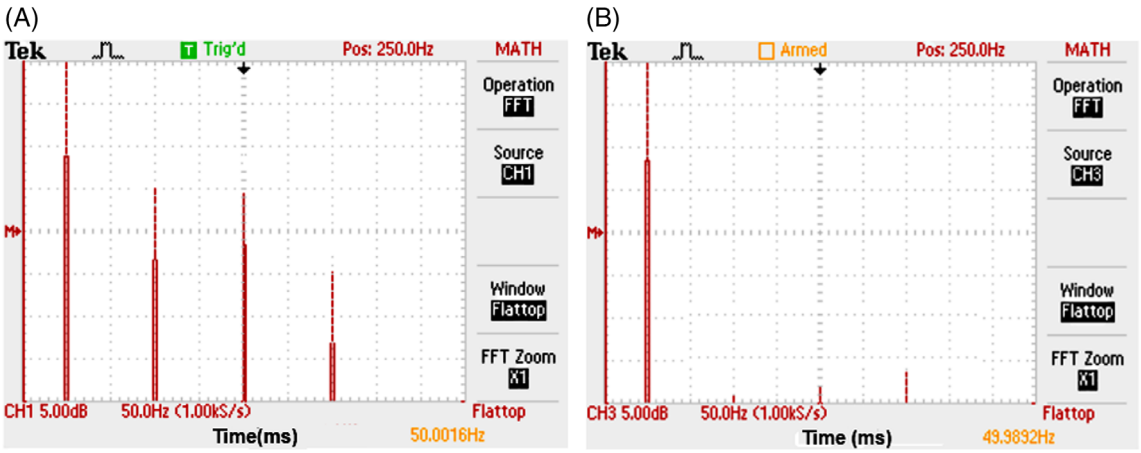


FIGURE 16 Experimental results of THD for case 1: load current harmonic distortions (A) without modular statcom

$$I_{p\,total} = \frac{Ip_L}{3} + I_{loss} \tag{29}$$

$$I_{q\,total} = I_{qq} - \frac{Iq_L}{3} \tag{30}$$

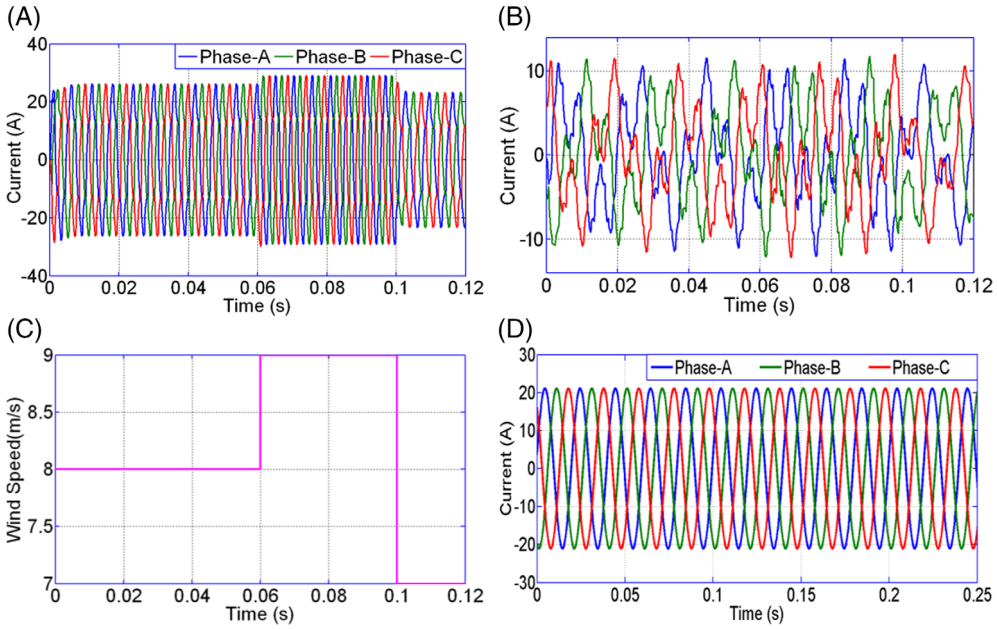


FIGURE 17 (A) Load current before compensation; (B) injected compensation current from modular statcom; (C) wind speed; and (D) source current

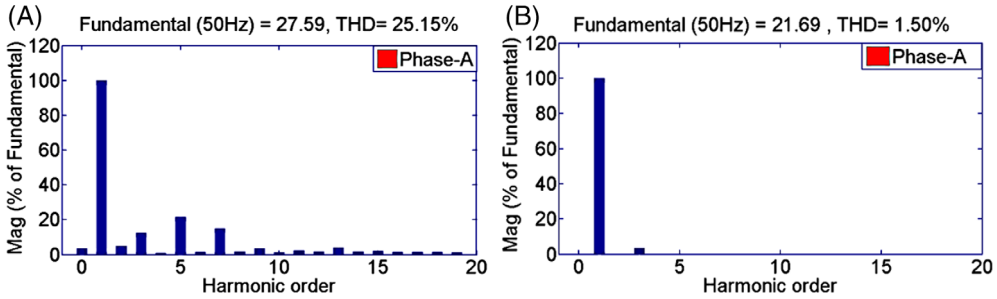


FIGURE 18 Simulation results of THD of load current for case 2: (A) without modular statcom

The reference currents I^*_{sa}, I^*_{sb},I^*_{sc} are obtained by multiplying the obtained total active and reactive current components with their respective in phase and quadrature voltage templates.

$$i^*_{sa} = I_{pLTotal} W_{pa} + I_{qLTotal} W_{qa} \tag{31}$$

$$i^*_{sb} = I_{pLTotal} W_{pb} + I_{qLTotal} W_{qb} \tag{32}$$

$$i^*_{sc} = I_{pLTotal} W_{pc} + I_{qLTotal} W_{qc} \tag{33}$$

These reference source currents are compared with the actual source currents and the error generated is transferred to the hysteresis controller. From the controller, the triggering pulses are obtained for the switches of the modular statcom. Figure 10 shows the flowchart of the proposed control system. From the flow chart, it is observed that the load current I_L is sensed and is given as input to the ESOGI from where the FC component of the load current is obtained. By implementing a zero-crossing detector (ZCD)[18] with sample and hold logic the in-phase and quadrature components

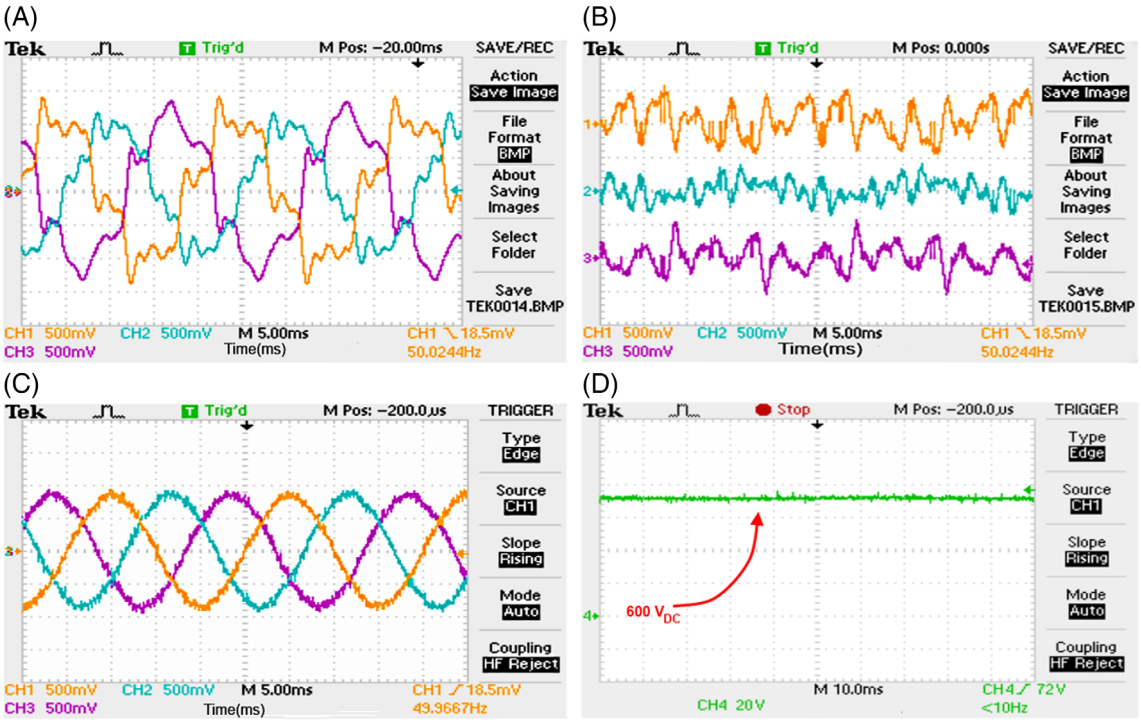


FIGURE 19 Experimental results of case 2 (A) load current without modular statcom; (B) injected compensation current; (C) source current with modular statcom; and (D) DC link voltage

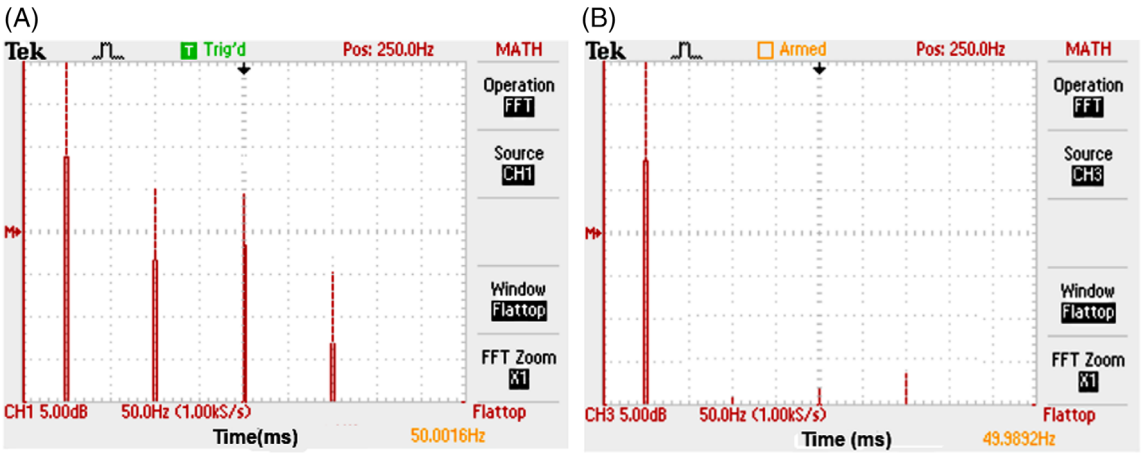


FIGURE 20 Experimental results of THD for case 2: load current harmonic distortions (A) without modular statcom; (B) with modular statcom

are derived from the FC. The role of sample and hold logic (S/H) is to obtain the active and reactive components from the load current.

4.1.3 | Control scheme for the flywheel energy storage

A PI controller is implemented for the flywheel storage system. Figure 11 displays the control system for Flywheel energy storage system. In order to compute the power error (P_{er}), the estimated power (P_{est}) is compared to the rated power (P_{rated}) of the generator. The power error (P_{er}) is given to the PI controller for control of the chopper. The output of the PI controller is compared to a carrier wave which results in the PWM output for the chopper switch with different duty cycles.

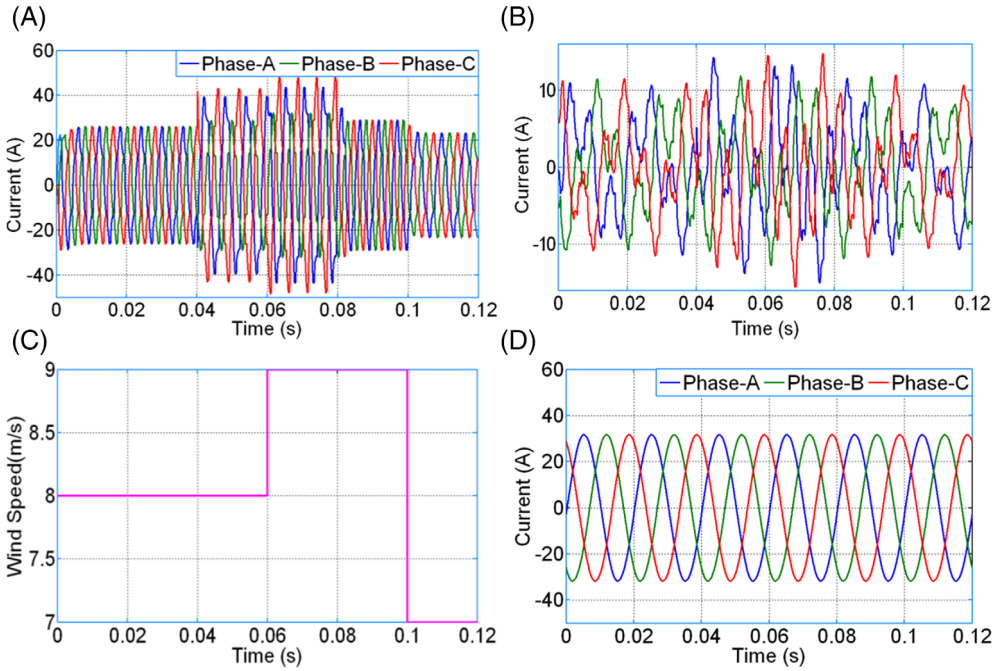
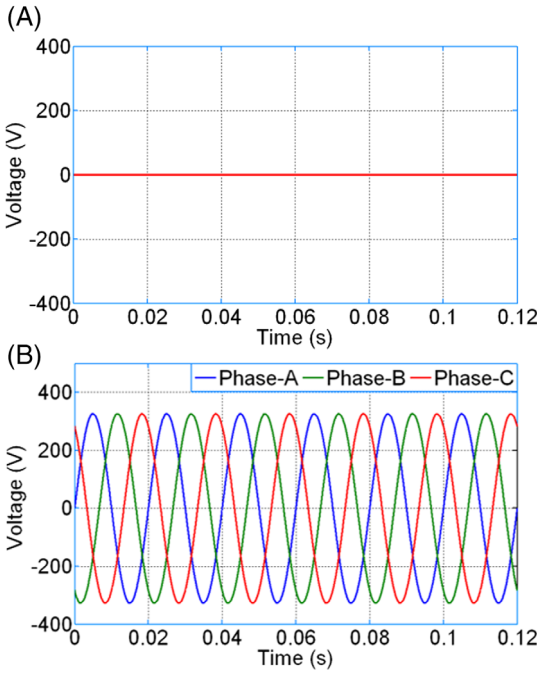


FIGURE 21 Simulation results for case 3: (A) load current; (B) injected compensation current; (C) wind speed; and (D) source current

FIGURE 22 Simulation results of wind blow failures: (A) source voltage with when there is no wind blow; (B) load voltage after connecting modular statcom



$$P_{er(n)} = P_{rated\,(n)} - P_{est(\,(n)} \tag{34}$$

4.2 | Performance comparison between ESOGI method and the conventional method.

The ESOGI method is compared with the other traditional SOGI and DSOGI (Dual SOGI), MSOGI (Multiple SOGI). Table 5 shows the comparison of the control methods. From Table 5, it is observed that the proposed method has a superior performance than other methods in terms of control complexity, accuracy, harmonic mitigation, and DC offset rejection.

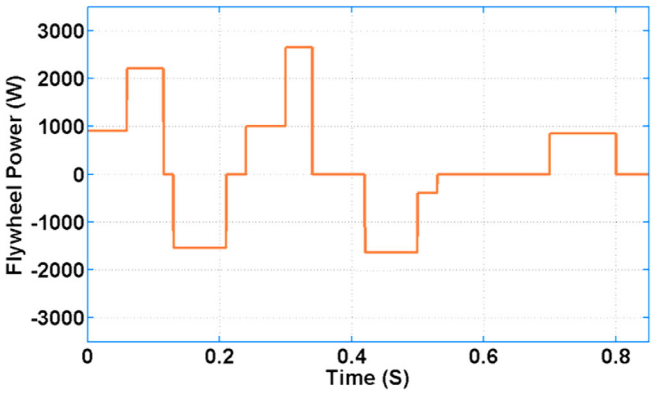


FIGURE 23 Output of the flywheel storage system

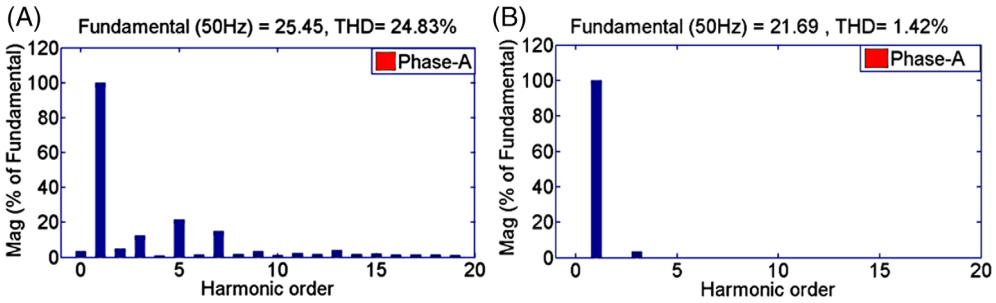


FIGURE 24 Simulation results of load current THD for case 3: (A) without modular statcom; (B) with modular statcom

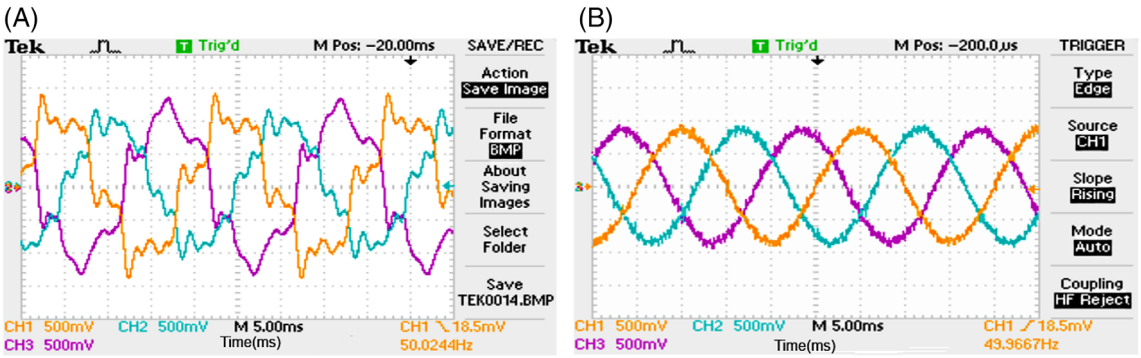


FIGURE 25 Experimental results of current compensation: (A) load current without modular statcom; (B) source current with modular statcom

5 | RESULTS AND DISCUSSIONS:

The PV-assisted modular statcom with (fuzzy logic controller) FLC is used to test the output under various load conditions using Matlab 2017a. Table 6 shows the simulation parameters of the proposed system. The input DC power to the inverter is in the ratio of 1:1:1:1, therefore each PV module with the implementation of landsman converter is scaled to 150 V DC. Combining all the four DC sources a peak value of 600 V DC is obtained as the DC link voltage of the modular statcom. In the various cases, the feasibility of the system proposed is evaluated. The results of the simulations are given in the following sections for different case studies.

5.1 | Case 1: balanced non-linear loads at constant wind speed

The modular statcom is evaluated in this case at constant wind speed under balanced linear loads. Figure 12 shows the simulation results of case 1.

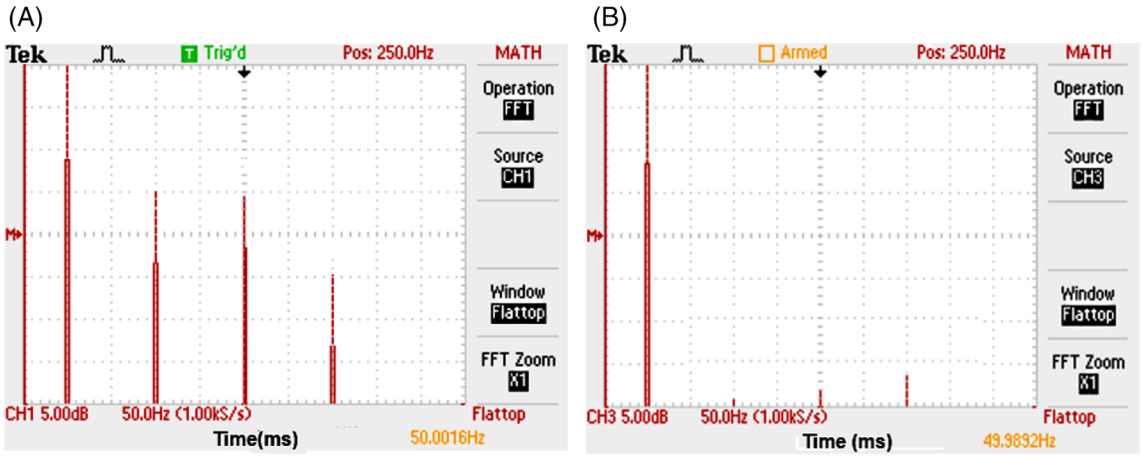


FIGURE 26 Experimental results of THD for case 3: load current harmonic distortions (A) without modular statcom; (B) with modular statcom

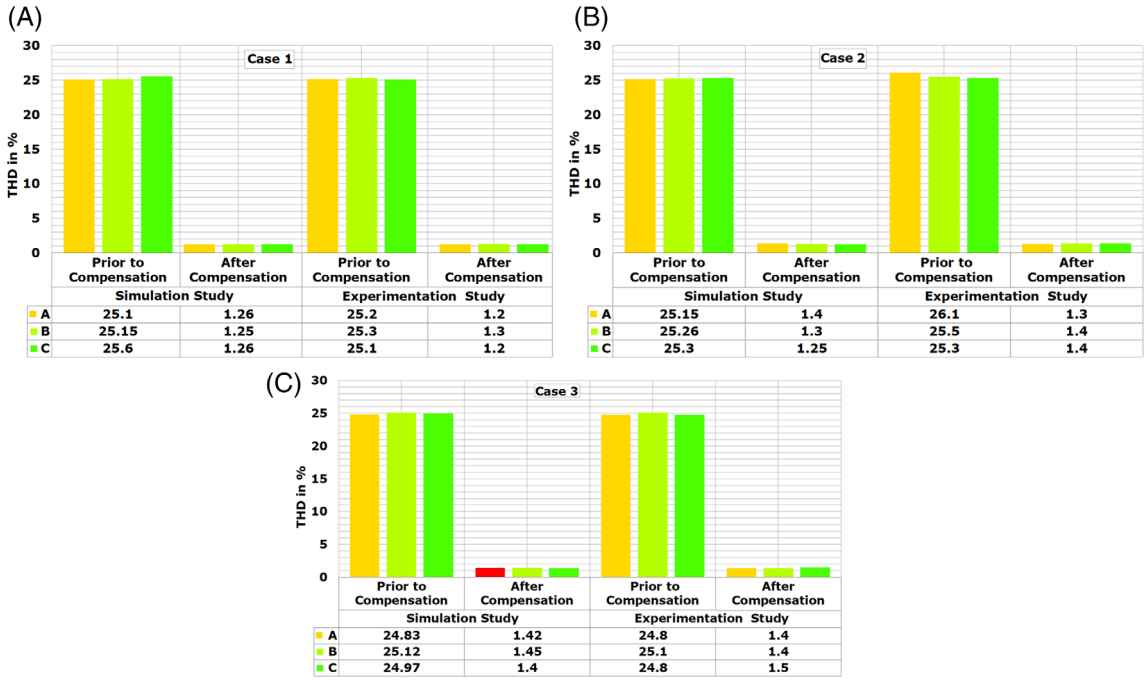


FIGURE 27 THD analysis of modular statcom before and after compensation for (A) case 1; (B) case 2; and (C) case 3

From Figure 12, it is observed that the modular statcom develops the compensated current and injects it at the PCC so that the harmonic currents evolved during the switching of non-linear load gets canceled and makes the source current sinusoidal. Figure 13 shows the current THDs of the proposed system without the use of PV-based modular statcom. Figure 14 shows the current THDs of the proposed system after implementing the PV-based modular statcom. From Figures 13 and 14, it is observed that there is a huge reduction in current THD of the system when modular statcom is activated. Figure 15 shows the experimental results for case 1 and Figure 16 presents the THD of the load current before and after implementing the modular statcom. From the results, it is evident that the load current harmonics are nullified using the modular statcom. The compensation currents of individual phases presented in Figure 15B is responsible for the mitigation of harmonics and makes the source current sinusoidal, as observed in Figure 15C. From Figure 16A, it is observed that the lower order harmonics is very high and is denoted as the worst case (without using the modular statcom). The third, fifth, and seventh order harmonics are extremely dangerous and

TABLE 7 Simulation and experimental THD values with and without modular statcom

	Simulation Voltage THD (%)									Experimental Voltage THD (%)					
	Without modular statcom			Modular statcom E-SOGI			Modular statcom with FLC based E-SOGI			Without modular statcom			With modular statcom		
Phase	Case: 1	Case: 2	Case: 3	Case: 1	Case: 2	Case: 3	Case: 1	Case: 2	Case: 3	Case: 1	Case: 2	Case: 3	Case: 1	Case: 2	Case: 3
A	22.4	24.2	23.2	2.63	2.64	2.75	1.22	1.20	1.23	22.50	23.10	22.30	1.2	1.2	1.3
B	23.0	23.7	24.6	2.72	2.68	2.77	1.21	1.19	1.21	23.45	23.15	23.60	1.2	1.1	1.2
C	23.2	24.1	24.1	2.65	2.72	2.81	1.20	1.21	1.21	24.10	23.50	24.50	1.1	1.2	1.2

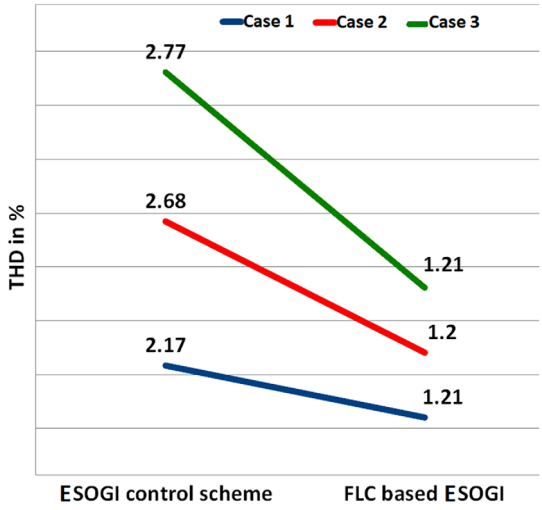


FIGURE 28 THD values of the proposed system using ESOGI and FLC based ESOGI

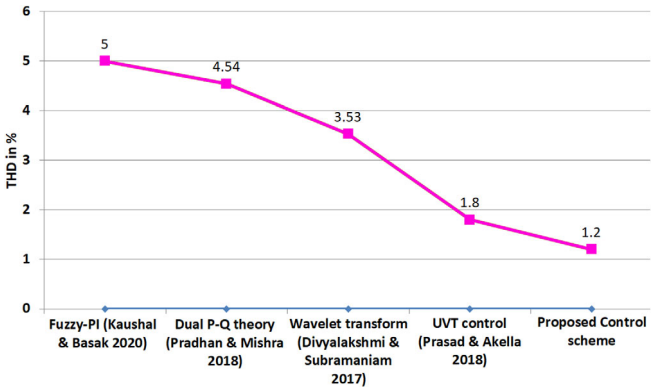


FIGURE 29 Performance analyses for the various harmonic compensation schemes

will damage the entire system. In Figure 16B, it is observed that implementing the modular statcom the lower harmonics are reduced. The use of modular statcom for harmonic mitigation is denoted as the best case. The obtained THD for the worst and best case is 25% and 1.2%.

5.2 | Case 2: balanced non-linear loads at varying wind speed

The simulation outputs for case 2 is presented in Figures 17 and 18, the THD of the load current before and after connecting the modular statcom. Figure 17A presents an asymmetric load current with harmonic content. This scenario exists when the non-linear load is switched on from 0.06 to 0.1 ms. Figure 17B shows the output of the compensation current which interacts with the load current at PCC and makes it sinusoidal. Therefore, the source current is protected from the harmonics by introducing the compensation current. Figure 17D shows the output of the distortion less source current. Figure 19 shows the experimental results of the case 2. Figure 20 shows the THD of the load current before and after connecting the modular statcom. It is observed that the THD obtained in the worst case and best case is 25% and 1.4%.

5.3 | Case 3: unbalanced non-linear loads at varying wind speed

The simulation outputs for the proposed system for case 3 are presented in Figure 21, which includes load current, injected compensation current from modular statcom, varying wind speed and the source current. From Figure 21, the efficiency of modular statcom is analyzed under unbalanced non-linear load at a varying wind speed. During the time

from 0.04 to 0.08 second, the unbalanced load is applied. The modular statcom responds to this situation and balances the load current that maintains the equilibrium of source current and source voltage at the SEIG terminal. When the WECS is under maintenance, the PV system provides the supply to the load. Figure 22 shows the output of WECS under maintenance and the load voltage after connecting modular statcom. Figure 23 shows the output of the flywheel storage system. The THD of the load current with and without the modular statcom is presented in Figure 24. Figure 25 shows the experimental output of load current with and without the modular statcom. Figure 26 shows the current THD of the proposed system with and without the modular statcom. Figure 27 shows the THD comparison of both the simulation and experimental studies for the case 1, case 2, and case 3. Table 7 shows the simulation and experimental THD values of the voltage of individual phases with and without the modular statcom. Figure 28 shows the graphical representation of THD values of the proposed system with ESOGI- and FLC-based ESOGI.

Figure 29 shows the performance analysis of various harmonic mitigation schemes with the proposed method. From Figure 29, it is evident that the proposed FLC-based ESOGI removes the harmonics in the system at PCC and makes the source current sinusoidal. From the above results, it is evident that the modular statcom with FLC-based ESOGI can eliminate current harmonics. The comparative study with the existing method clearly indicates that a harmonic distortion in the source current measured by the proposed system is 1.2%, which is below the average THD level obtained by the systems of Kausal and Basak[19]; Piradhan and Mishra[20]; Divyalakshmi and Subramaniam[21]; and Prasad and Akella.[22]

6 | CONCLUSION

A WECS supported by PV-fed modular statcom connected to a non-linear load is simulated in Matlab 2017a and experimentally developed in the laboratory. The prototype is tested under various cases. The ESOGI method is effectively implemented for control of the output power. The power quality of the system is increased, along with voltage regulation, as the THDs on generated voltages and currents remain mostly within the IEEE-519 standard limits. Comparison of the ESOGI method with the standard SOGI, DSOGI, and MSOGI is provided. The proposed system can be used for both stand-alone and grid-connected systems. Furthermore, a strong dynamic response and better ability to eliminate DC offset than traditional SOGI-based control are demonstrated in the proposed ESOGI-based control.

PEER REVIEW

The peer review history for this article is available at https://publons.com/publon/10.1002/2050-7038.12845.

DATA AVAILABILITY STATEMENT

The data that support the findings of this study are available on request from the corresponding author. The data are not publicly available due to privacy or ethical restrictions.

ORCID

Dishore Shunmugham Vanaja https://orcid.org/0000-0002-7581-2164
Albert Alexander Stonier https://orcid.org/0000-0002-3572-2885

REFERENCES

1. Albert JR, Stonier AA. Design and development of symmetrical super-lift DC–AC converter using firefly algorithm for solar-photovoltaic applications. *IET Circuits, Devices Syst*. 2020;14(3):261-269.
2. Shunmugham Vanaja D, Stonier A. A novel PV fed asymmetric multilevel inverter with reduced THD for a grid-connected system. *Int Trans Electr Energy Syst*. 2020;30(4):1-25.
3. Wang J, Bo D, Miao Q, Li Z, Wu X, Lv D. Maximum power point tracking control for a doubly fed induction generator wind energy conversion system based on multivariable adaptive super-twisting approach. *Int J Electr Power Energy Syst*. 2021;124:106347.
4. Shunmugham Vanaja D, Stonier AA. Grid integration of modular multilevel inverter with improved performance parameters. *Int Trans Electr Energy Syst*. 2021;31(1):e12667.
5. Zhang G, Hu W, Cao D, et al. Deep reinforcement learning based approach for proportional resonance power system stabilizer to prevent ultra-low-frequency oscillations. *IEEE Trans Smart Grid*. 2020;11(6):5260–5272.
6. Tiwari VK, Gupta AR. Application of SVC and STATCOM for wind integrated power system. *Recent Advances in Power Electronics and Drives*. Singapore: Springer; 2021:181-192.

7. Zhang G, Hu W, Cao D, et al. A data-driven approach for designing STATCOM additional damping controller for wind farms. *Int J Electr Power Energy Syst*. 2020;117:105620.
8. Samala RK, Mercy Rosalina K. Optimal allocation of multiple photo-voltaic and/or wind-turbine based distributed generations in radial distribution system using hybrid technique with fuzzy logic controller. *J Electr Eng Technol*. 2021;16:101-113.
9. Cao D, Hu W, Zhao J, Huang Q, Chen Z, Blaabjerg F. A multi-agent deep reinforcement learning based voltage regulation using coordinated PV inverters. *IEEE Trans Power Syst*. 2020;35(5):4120-4123.
10. Narendran A, Sureshkuma R. Hysteresis-controlled-landsman converter based multilevel inverter fed induction-motor system using PIC. *Microprocess Microsyst*. 2020;76:103099.
11. Kumar V, Singh M. Derated mode of power generation in PV system using modified perturb and observe MPPT algorithm. *J Mod Power Syst Clean Energy*. 2020;1-10.
12. Albert JR, Vanaja DS. Solar energy assessment in various regions of Indian sub-continent. *Solar Cells*. London, SW7 2QJ, United Kingdom: IntechOpen; 2020.
13. Babaei E. A cascade multilevel converter topology with reduced number of switches. *IEEE Trans Power Electron*. 2008;23(6):2657-2664.
14. Chaudhuri T, Rufer A. Modeling and control of the cross-connected intermediate-level voltage source inverter. *IEEE Trans Ind Electron*. 2010;57(8):2597-2604.
15. Chaudhuri T, Rufer A, Steimer PK. The common cross-connected stage for the 5L ANPC medium voltage multilevel inverter. *IEEE Trans Ind Electron*. 2010;57(7):2279-2286.
16. Khoun Jahan H, Abapour M, Zare K. Switched-capacitor-based single-source cascaded H-bridge multilevel inverter featuring boosting ability. *IEEE Trans Power Electron*. 2018;34(2):1113-1124.
17. Gupta S. Fuzzy logic control D-STATCOM technique. Paper presented at: Proceedings of International Conference on Artificial Intelligence and Applications; 2021. Singapore: Springer. pp. 173-183.
18. Chandran VP, Murshid S, Singh B. Design and analysis of improved second order generalized integrator-based voltage and frequency controller for permanent magnet synchronous generator operating in small-hydro system feeding single-phase loads. *Int Trans Electr Energy Syst*. 2019;29(5):e2827.
19. Kaushal J, Basak P. Power quality control based on voltage sag/swell, unbalancing, frequency, THD and power factor using artificialneural network in PV integrated AC microgrid. *Sustainable Energy, Grids Netw*. 2020;23:100365.
20. Pradhan M, Mishra MK. Dual P-Q theory based energy-optimized dynamic voltage restorer for power quality improvement in a distribution system. *IEEE Trans Ind Electron*. 2018;66(4):2946-2955.
21. Divyalakshmi D, Subramaniam NP. Photovoltaic based DVR with power quality detection using wavelet transform. *Energy Procedia*. 2017;117:458-465.
22. Prasad M, Akella AK. Voltage and current quality improvement by solar photovoltaic fed ZSI-DVR. *Procedia Comput Sci*. 2018;125:434-441.

How to cite this article: Shunmugham Vanaja D, Albert JR, Stonier AA. An Experimental Investigation on solar PV fed modular STATCOM in WECS using Intelligent controller. *Int Trans Electr Energ Syst*. 2021;31:e12845. https://doi.org/10.1002/2050-7038.12845